Advanced Composites and Hybrid Materials (2023) 6:166
https://doi.org/10.1007/s42114-023-00738-w

RESEARCH

Two-dimensional superlattice films of gold nanoparticle-polystyrene composites: a bioactive platform for bone homeostasis maintenance

Zaikai Zhuang[1] · Zheng Li[2] · Guangyu Gong[3] · Qiangqiang Li[1] · Yibo Zhang[1] · Caoxing Huang[4] · Yusen Huang[3] · Lei Tian[5] · Peng Wang[1,2,6,7] · Zhirui Guo[6] · Qing Jiang[1,6,7]

Received: 30 May 2023 / Revised: 18 August 2023 / Accepted: 27 August 2023

Abstract
Osseo-integration between the implant and bone is a crucial factor to create a strong, durable bond that allows the implant to function effectively. However, regular implant surface with poor osseo-integration ability may cause aseptic loosening, resulting in the failure of implants. Herein, a serial of macroscopic one-particle thick superlattice films generated by self-assembly of diverse size of gold nanoparticles (GNPs) were termed as SFGs and were considered as bioactive implant coatings for enhancing osseo-integration. A hydroquinone-assisted seed method is established to fabricate homogenous GNPs with controllable sizes (20, 60, and 90 nm), which were further employed as building blocks to generate macroscopic one-particle thick superlattice films of GNPs (SFGs-20, SFGs-60, and SFGs-90) with the assistance of ploystryrene. The SFGs present a size-dependent performance on bone homeostasis, where SFGs-90 demonstrated the most pronounced facilitation of osteogenic differentiation of osteoblasts as well as deactivation of osteoclasts compared with SFGs-20 and SFGs-60. Considering the universal applicability of SFGs for depositing on various substrates, these SFGs with enhanced osseo-integration capabilities could serve as a bioactive platform for surface modification of orthopedic implants, effectively addressing the issue of aseptic loosening.

Keywords Gold nanoparticles · Polystyrene · Self-assembly · Aseptic loosening · Superlattice films · Osseo-integration

1 Introduction

Aseptic loosening is a prevalent cause of orthopedic implant failure marked by pain and implant mobility. It often results from the lack of bone ingrowth in the early postoperative period, which subsequently leads to the gradual loss of attachment between the implant and surrounding bone tissue [1]. Two main factors can contribute to aseptic loosening, including poor osseo-integration of orthopedic implants and the chronic low-grade aseptic inflammatory response triggered by wear particles generated by the prosthetic implant [2]. Specifically, poor osseo-integration creates a

Zaikai Zhuang, Zheng Li, and Guangyu Gong contributed equally to this work, regarding as the first author.

✉ Peng Wang
15850681759@163.com

✉ Zhirui Guo
zhiruiguo@njmu.edu.cn

✉ Qing Jiang
qingj@nju.edu.cn

[1] Division of Sports Medicine and Adult Reconstructive Surgery, Department of Orthopedic Surgery, Nanjing Drum Tower Hospital Clinical College of Nanjing Medical University, 321 Zhongshan Road, Nanjing, Jiangsu 210008, People's Republic of China

[2] State Key Laboratory of Bioelectronics, Jiangsu Key Laboratory for Biomaterials and Devices, School of Biological Science and Medical Engineering, Southeast University, Nanjing 210009, People's Republic of China

[3] Lab Center, The Second Affiliated Hospital of Nanjing Medical University, Nanjing 210029, People's Republic of China

[4] Co-Innovation Center for Efficient Processing and Utilization of Forest Resources, College of Chemical Engineering, Nanjing Forestry University, Nanjing 210037, People's Republic of China

[5] Department of Chemical Engineering, McMaster University, Hamilton, ON L8S 4L7, Canada

[6] Jiangsu Engineering Research Center for 3D Bioprinting, Nanjing, People's Republic of China

[7] Institute of Medical 3D Printing, Nanjing University, Nanjing, People's Republic of China

Published online: 16 September 2023

weak interface between the implant and the bone, leading to the micromotion and instability of orthopedic implants. This micromotion can result in prosthesis wear, which can enter into the gap between bone and implant, causing adipose tissue to break down, release cytokines. Subsequently, osteoclasts are activated and bone resorption was stimulated, resulting in osteolysis between bone and the implant and weakening of the bone-implant interface [3]. Increased severity in implant looseness results in a higher number of wear particles within the gap between bone and implants. This, in turn, exacerbates the wear of the implant, leading to further looseness and creating a destructive cycle. Hence, it is highly desirable and a great challenge to improve the osteo-integration with a stable and long-lasting interface between the implant for ensuring the long-term stability and success of orthopedic implants.

To date, a great number of efforts, including renewal of implant materials, surface modification, and porosity treatment, have been made to improve the osteo-integration (e.g., osteo-conductivity and osteo-inductivity) of orthopedic implants to avoid possible aseptic loosening [4]. Among these, surface modification has become a powerful and versatile tool to endow the current orthopedic implants with enhanced osseointegration ability [5]. Hydroxyapatite (HA) has been used for surface modification of orthopedic implants through plasma spraying method and the HA coating indeed improves the bone ingrowth and their long-term survival but still has some limitations such as relatively low corrosion resistance and poor binding force of the bone/implant interface [6]. Besides, alleviation of early inflammatory responses and enhancement of mineralized nodules formation could be achieved by surface modification of nano-patterning towards titanium implant using colloidal lithography [7]. Previous study demonstrated that the nanoscale surface modification of magnesium alloys consisted of magnesium hydroxide, stearic acid, and poly (1,3-trimethylene carbonate)) exhibited enhanced implant corrosion resistance and better biocompatibility [8]. The superior orthopedic implants are expected to be surface-modified with bioactive materials that possess enhanced osseo-integration ability, leading to the high binding strength towards native bone tissue.

Manipulation of stem cell fate has been the focus of significant interest in developing bioactive materials and nanotechnologies for various applications such as stem cell therapy and tissue regeneration [9]. The fate of stem cells can be tightly regulated by biophysical signals such as matrix stiffness, surface morphology, mechanical forces, and roughness of the bioactive materials [10]. Recently, there are accumulating evidences showing that interactions between biological cells and biomaterial nanostructured surface patterns could modulate fate of cells towards desired differentiation direction such as osteogenesis or adipogenesis [11]. Thus, it is of great significance to surface modification of the micro-topography patterns towards implant surface to exert suitable stimulation to biological cells, thereby regulating the fate of stem cells. Recently, Au-based films (e.g., films incorporated with GNPs) with high surface area and plasmonic effects can interact with light or other external stimuli, allowing for non-invasive, light-driven therapies [12–14] as well as some biomedical applications such as photocatalysts and antibacterial properties [15–17]. Besides, previous studies have demonstrated that the GNPs can facilitate osteogenic differentiation of biological cells [18]. Hence, the GNPs within the films can be released in a controlled manner, providing localized and sustained delivery to the bone site and helping stimulate bone cell proliferation and differentiation [19]. Apart from above Au-based films, two-dimensional (2D) composites assembled in a controllable way are considered to be very promising platforms for various applications [20–22]. Previous study reported that 2D layer-by-layer assembled gold nanoparticle films demonstrated controllable thermogenic effect in the presence of an alternating magnetic field, which could be for drug release of loaded hydrogels [23]. However, the nanoparticles in these 2D films were in aggregated state due to the present of poly-diallyldimethylammoniumchloride, which may have potential toxicity to living body. To date, free-standing 2D superlattice films of GNPs-polystyrene composites by drying-mediated bottom-up self-assembly strategy in a controllable way have attracted considerable attention in various applications such as cancer therapy (e.g., photothermal therapy (PTT) and drug delivery) [24], bio-sensing (e.g., detection of biomolecules and disease markers) [25], bio-imaging (e.g., SERS imaging and X-ray CT imaging) [26], and electromagnetic composites [27–29]. There are several advantages for superlattice films of GNPs: (i) its universality for depositing on diverse substrates; (ii) the morphology can be regulated in a controllable way by varying shape, size, or surface modification of GNPs; and (iii) unique fundamental properties such as high mechanical strength. Till now, to the best of our knowledge, the effects of superlattice films assembled with various sizes of GNPs on osteo-integration abilities remain unexplored.

In this study, three kinds of GNPs with average sizes of 20, 60 and 90 nm were prepared using citrate reduction and hydroquinone (HQ)-assisted seed-mediated growth method, where HQ was adopted because it can reduce Au precursors in the presence of preformed gold seeds at room temperature for size-controllable synthesis of citrate-stabilized spherical Au nanoparticles [30]. Subsequently, thiolated polystyrene (SH-PS) was used as binding ligand of GNPs for generating two-dimensional superlattice films of GNPs through physical entanglement between PS ligands during a drying-mediated self-assembly process [31]. Three kinds of 2D superlattice films of GNPs-polystyrene composites

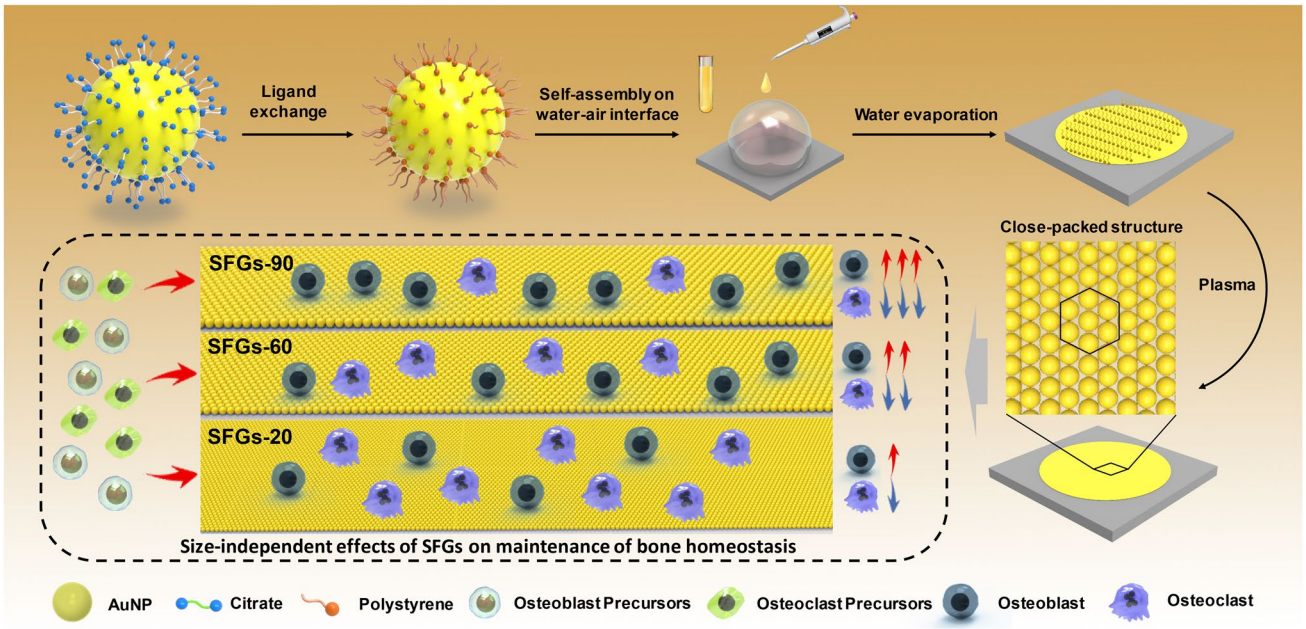

Scheme 1 Schematic of the preparation of SFGs for positive maintenance of bone homeostasis

(SFGs-20, SFGs-60, and SFGs-90) were considered as multifunctional bioactive interface for promoting osteogenic differentiation of osteoblasts as well as deactivating osteoclasts. To test this, their biocompatibility through live/dead staining and phalloidin/DAPI staining were firstly investigated. Subsequently, the effects of SFGs on osteogenic stimulation of osteoblasts were evaluated by detecting the expression of osteogenic-related genes, proteins, and alkaline phosphatase (ALP) immunofluorescence staining. Their osteoclastogenic inhibition effects on osteoclasts through analyzing the expression of osteoclastic-related genes, proteins, and tartrate-resistant acid phosphatase (TRAP) immunofluorescence staining were further examined. Together with the fact that the advantage of SFGs is its universality for depositing on various substrates (e.g., orthopedic implants), SFGs with excellent biocompatibility, pro-osteogenesis, and anti-osteoclastogenesis abilities could be considered as potential candidates for surface modification of orthopedic implants to avoid possible aseptic loosening (Scheme 1).

2 Materials and methods

2.1 Materials

Chloroform ($CHCl_3$), hydrogen tetrachloroaurate ($HAuCl_4 \cdot 4H_2O$, 99%), trisodium citrate ($C_6H_5Na_3O_7 \cdot 2H_2O$), and tetrahydrofuran (THF) were obtained from Shanghai Chemical Reagent Co., Ltd. (China). Hydroquinone (HQ) was received from Aldrich Chemical Co., Ltd. Thiol-functionalized polystyrene (Mn = 50,000 g/mol) was obtained from Polymer Source, Inc. Demineralized water was purified with a Milli-Q system (Millipore). The detailed properties and applications of the used reagents and antibodies in cell experiment are shown in Table S1.

2.2 Preparation of NPs with various sizes

The GNPs were prepared by a citrate reduction and hydroquinone-assisted seed-mediated growth method. The size of as-prepared GNPs was expected to range from 15 to 100 nm by altering the condition of synthesis [32]. Detailed preparation method could be seen in Supplementary material.

2.3 Fabrication of 2D SFGs

To fabricate the SFGs-20, 20 mL of GNPs-20 was centrifuged at 10,000 g for 30 min. After that, the samples were redispersed into THF (5 mL) containing SH-PS (20 mg, 4 mg/mL). The solution was kept in dark for 3 h. Then, the NPs were washed with THF and $CHCl_3$ (8600 g, 12 min) by turns. A water droplet was deposited on a substrate and subsequently a 0.5 μL droplet of GNPs-20/$CHCl_3$ was spread on the water/air interface. The evaporation of the solvent result in the formation of a monolayer SFGs. For SFGs on silicon wafers, a concentrated droplet (0.7 μL) of GNPs-20/ $CHCl_3$ was used to fabricate SFGs. For SFGs on 6-well plates, a concentrated droplet (0.8 μL) of GNPs-20/$CHCl_3$ was dropped

onto the surface of a large water droplet on a 6-well plate for 9 times until covering almost the 6-well plate.

To fabricate SFGs-60, 60 nm GNPs (20 mL) was centrifuged at 2800 g for 14 min. After that, the samples were redispersed into THF (5 mL) containing 20 mg of SH-PS (20 mg, 4 mg/mL). The solution was kept in dark for 3 h. Then, the NPs were washed with THF and $CHCl_3$ (8600 g, 12 min) by turns. The remaining fabrication process kept the same for SFGs-20.

To fabricate SFGs-90, 90 nm GNPs (30 mL) was centrifuged at 1000 g for 10 min and redispersed into 5 mL of THF containing 20 mg of SH-PS (4 mg/mL). The solution was kept in dark for 3 h. Then, the NPs were washed with THF and $CHCl_3$ (8600 g, 12 min) by turns. The remaining fabrication process kept the same for SFGs-20.

2.4 Characterization

The surface morphology of samples was observed on a transmission electron microscopy (TEM, JEM-2100, Japan), field-emission scanning electron microscope (FE-SEM, Zeiss Supra 40 Gemini, Germany), and atomic force microscopy (AFM, Signal Hill, CA, USA). The extinction and mirror reflectance spectra were recorded on a UV-vis-NIR spectrophotometer (Shimadzu, UV-3600, Japan). The size of GNPs was measured by dynamic light scattering (Malvern Zetasizer Nano ZS90, UK). The rheological property of the PEG hydrogel was assessed on a Modular Advanced Rheometer System (Thermo Scientific HAAKE MARS, USA).

2.5 Plasma treatment

Brief plasma exposures can remove impurities and tarnish from SFGs. For plasma treatment, the as-prepared SFGs assembled on 6-well plates were place in a Harrick PDC-002 Plasma Cleaner for 5 min, in which air was used as media and absolute pressure was set to 0.65 Torr (1 Torr = 133.322 Pa).

2.6 Biocompatible assessment

MC3T3-E1 and RAW264.7 cells were cultured on SFGs-20, SFGs-60, SFGs-90, and the blank wells (used as controls) for 24 h. Live/dead staining and phalloidin/DAPI staining were performed to assess cell viability and morphology, respectively. Live/dead staining was performed using the live/dead double-staining kit (KGAF001, KeyGEN BioTECH, China) and involved washing the cells with PBS, followed by staining with propidium iodide (PI, 8 μM) and calcein-AM (2 μM) for 30 min. Live cells stained by green using calcein-AM, which were distinguished from dead cells stained red with PI under fluorescence microscopy. For phalloidin/DAPI staining, the cells were fixed using 4% paraformaldehyde and subsequently permeabilized with 0.5% Triton X-100 in PBS. For visualization, F-actin and nuclei were stained green with fluorescein (FITC) phalloidin (F432, 1:400, Thermo Fisher Scientific, USA), and blue with DAPI (ab104139, Abcam, USA), respectively.

2.7 Cell culture

The MC3T3-E1 cell line was employed for osteogenic differentiation evaluation of SFGs. The cells were cultured in growth medium (GM), consisting of α-MEM medium (Gibco, USA) with 10% fetal bovine serum (FBS, Gibco, USA) and 1% penicillin–streptomycin (PS, Gibco, USA) at 37 °C in 5% CO_2. The culture medium was replaced every 3 days. RAW264.7 cells were used for osteoclast differentiation and were cultured in high-glucose DMEM medium supplemented with 10% FBS and 1% PS at 37 °C in 5% CO_2. The culture medium was changed every 2 days, and the cells were harvested for subsequent experiments when they reached 70–80% confluency.

2.8 Induction and evaluation of osteogenic differentiation

MC3T3-E1 cells were cultured on SFGs-20, SFGs-60, SFGs-90, and the blank well. Once the cells grew to 80% full, the culture mediums were replaced by osteogenic mediums (OM) consisted of GM supplemented with ascorbic acid (50 μg/mL), dexamethasone (0.1 μM), and β-glycerophosphate (10 mM) to induce osteogenic differentiation. Several tests were performed to evaluate the effectiveness of the differentiation process, including alkaline phosphatase (ALP) activity assay, ALP immunofluorescence staining, quantitative PCR, and Western blotting. Quantitative PCR was used to detect mRNA expression levels of osteocalcin (OCN), osteopontin (OPN), collagen I (Col1), ALP, and Runt-related transcription factor 2 (Runx2). The forward and reverse primers are listed in Table S2. Protein levels were analyzed with Western blotting using primary antibodies against OCN (23,418–1-AP, Proteintech, China), OPN (GB112328, Servicebio, China), COL-1 (ab260043, Abcam, USA), ALP (A0514, ABclonal, China), and RUNX2 (ab23981, Abcam, USA). HRP-conjugated secondary antibodies from Biosharp, Hefei, China, were also used in the analysis. Detailed methods for quantitative real time-PCR and Western blotting could be seen in Supplementary material.

2.9 ALP activity assay and ALP immunofluorescence staining

MC3T3-E1 cells were cultured on SFGs-20, SFGs-60, SFGs-90, and the blank well. Following a 7-day osteogenic

induction process, ALP activity levels as an indicator of osteogenic differentiation were detected in the cells on various substrates. Alkaline Phosphatase Assay Kit (Beyotime, China) was utilized to detect ALP activity levels. To perform the ALP immunofluorescence staining, cells were washed with PBS twice, and subsequently fixed with 4% paraformaldehyde for 30 min. After washed with PBS for 2 times, the cells were permeabilized for 30 min using 0.5% Triton X-100, followed by being blocked at room temperature for 1 h with 1% BSA in PBS. After being washed with PBS for two times, the cells were incubated with rabbit ALP antibodies (A0514, 1:200, Abclonal, China) diluted in 1% BSA overnight at 4℃. The cells were washed in PBS and again incubated with secondary antibodies, AlexaFluor 488 goat anti-rabbit IgG (H+L) (AFSA005, 1:200, AiFang Biological, China), for 1 h at room temperature and protected from light. Nuclei were then stained with mounting medium containing DAPI (ab104139, Abcam, USA) and the cells were visualized under a fluorescence microscope.

2.10 Induction and evaluation of osteoclastic differentiation

RAW264.7 cells were incubated on SFGs-20, SFGs-60, SFGs-90, and the blank wells. In order to induce osteoclastic differentiation, the cells were switched to osteoclastic differentiation medium consisting of high-glucose DMEM medium supplemented with 10% FBS, 1% PS, M-csf (50 ng/mL), and RANKL (50 ng/mL). TRAP immunofluorescence staining, quantitative PCR, and Western blotting were performed to evaluate osteoclastic differentiation. The mRNA expressions levels of nuclear factor of activated T cells, cytoplasmic 1 (NFATC1), TRAP, Matrix metalloproteinase 9 (MMP9), ATPase H+ transporting V0 subunit D2 (ATP6vOd2), Fos proto-oncogene AP-1 transcription factor subunit (c-Fos), Cathepsin K (CTSK), and tumor necrosis factor receptor-associated factor 6 (TRAF6) were detected by quantitative PCR at 3 and 5 days in osteoclastic differentiation medium (primers are listed in Table S3). And the protein levels were analyzed by Western blot at 3 days in osteoclast differentiation medium. The primary antibodies used were as follows: NFATC1 (AF06823, AiFang biological, China), TRAP (11,594–1-AP, Proteintech, China), c-Fos (31254S, Cell Signaling Technology, USA), CTSK (A1782, abclonal, China), and TRAF6 (A16991, abclonal, China). The horseradish peroxidase (HRP) conjugated secondary antibodies were from Biosharp, Hefei, China.

2.11 TRAP immunofluorescence staining

Primary bone marrow monocytes (BMMs) were isolated from 8-week-old C57BL/6 mice and cultured in high-glucose DMEM medium supplemented with 10% FBS, 1% PS, M-csf (50 ng/mL). Once the cell density reached 90–100%, the cells were cultured in osteoclast medium (high-glucose DMEM medium supplemented with 50 ng/mL M-CSF and 50 ng/mL RANKL) to induce differentiation. Cell culture media were replaced every 2 days until osteoclast formation. Differentiated cells cultured on four different substrates were evaluated by fluorescence staining of TRAP, F-actin, and nuclei. The nucleus was stained in blue with DAPI (ab104139, Abcam, USA), actin labeled in red with phalloidin (RM02835, 1:100, Abclonal, China), and TRAP were stained in green. The primary antibody used was ACP5 polyclonal antibody (25,104-1-AP, 1:200, Proteintech, China), and the specific steps were conducted as described in Sect. 2.8.

2.12 Statistical analysis

Differences among multiple groups were evaluated by one-way analysis of variance (ANOVA), followed by the Tukey's test. Statistical analysis was performed using GraphPad Prism 8, with $P < 0.05$ considered significant.

3 Results and discussion

3.1 Preparation and characterization of GNPs with various sizes

A key advantage of GNPs is their size and shape diversity, which can be controlled by varying the reaction parameters, including time, temperature, reductant types, and capping ligand types [33]. Here, citrate-modified GNPs with various sizes were firstly prepared using citrate reduction and seed-mediated growth method as described in a reported study [34]. Typical citrate method for GNPs includes the reduction of $HAuCl_4$ solution at boiling using citrate as both stabilizing and reducing agent. Unfortunately, particles larger than 20 nm obtained by citrate method were always poly-dispersed and non-spherical. While regrowing gold onto tiny nanoparticles (also called seeds) improves this, a large amount of secondary population of smaller nanoparticles is also generated. Therefore, hydroquinone-assisted seed method to fabricate homogenous GNPs with controllable sizes was employed. Hydroquinone (HQ) has a moderate reducing potential ($E^\circ = -0.699$ V vs NHE), which can quickly reduce Au precursor (AuCl4-/Au0, $E^\circ = +1.002$ V) at room temperature only in the presence metallic seeds [31]. Moreover, HQ and its oxidative product quinone give a poor adsorption to the NP surface, enabling it an exclusive reductant with minimal stabilizing effects.

Taking advantage of above two merits, we adopted citrate-stabilized Au NPs with controllable sizes by a seed-mediated approach in HQ reduction and the process

of preparation is schematically shown in Fig. 1A. Their morphology obtained by transmission electron microscopy (TEM) imaging is demonstrated in Fig. 1B–D, where it could be seen that the nanoparticles were spherical with better mono-dispersity. Their average statistical sizes calculated according to the TEM images were 21.18 ± 1.69 nm, 60.27 ± 5.57 nm, and 92.83 ± 9.38 nm, respectively (Fig. 1E). Average hydrodynamic sizes (Fig. 1F) measured by dynamic light scattering (DLS) were around 28 nm for GNPs-20, 65 nm for GNPs-60, and 99 nm for GNPs-90, respectively, the value of which was larger than their physical sized due to the citrate modification and the hydrated shell. In addition, the zeta (ζ) potential of these nanoparticles was negative charged with -24, -11.4, and -6.39 mV, respectively (Fig. 1G). The negative charge of as-prepared GNPs was attributed to the carboxyl groups of citrate molecule. The zeta potential value of nanoparticles depends on their surface charge density. Larger nanoparticles have a relatively smaller surface area, resulting in a higher surface charge density concentrated in a smaller region. In contrast, smaller nanoparticles have a relatively larger surface area, leading to a lower surface charge density distributed over a wider region [35]. It is generally accepted that the physiochemical properties, especially optical properties of GNPs, have significant relationship with their size [36].

In addition, UV-Vis spectroscopy of as-prepared GNPs with various sizes is further shown in Fig. 1H, in which sharp and single absorption band with the location of 519 nm for GNPs-20, 536 nm for GNPs-60, and 565 nm for GNPs-90, respectively. The red-shift of absorption band from GNPs-20 to GNPs-90 was attributed to the increase of effective refractive index resulted from the increased size [37]. Currently, it has become a widely accepted characterization program for confirming the sizes of GNPs through the combination of TEM observation and extinction spectra recording. The extinction spectra of three kinds of GNPs are seen to be in good agreement with the published data that calculated from Mie theory besides the TEM observation [38]. Taken together, it can be verified that the three kinds of GNPs are in sizes of 20 nm, 60 nm, and 90 nm, respectively. The as-prepared GNPs were of great reproducibility and could be used as building block for self-assembly of SFGs.

3.2 Preparation and characterization of SFGs

SFGs were constructed via a general two-step polystyrene (PS)-based drying-mediated self-assembly method at a convex air–water interface based on physical entanglement between ligands, where PS-modified GNPs were used as building block [30]. Before self-assembly, thiolated polystyrene (SH-PS) ligands with stronger binding ability were used to surface modification of citrate-capped GNPs, facilitating their transferring into an organic phase such as tetrahydrofuran (THF) [27]. Drying-mediated self-assembly of PS-capped GNPs could be accomplished by drop-casting them on various substrates such as holey copper grids (for

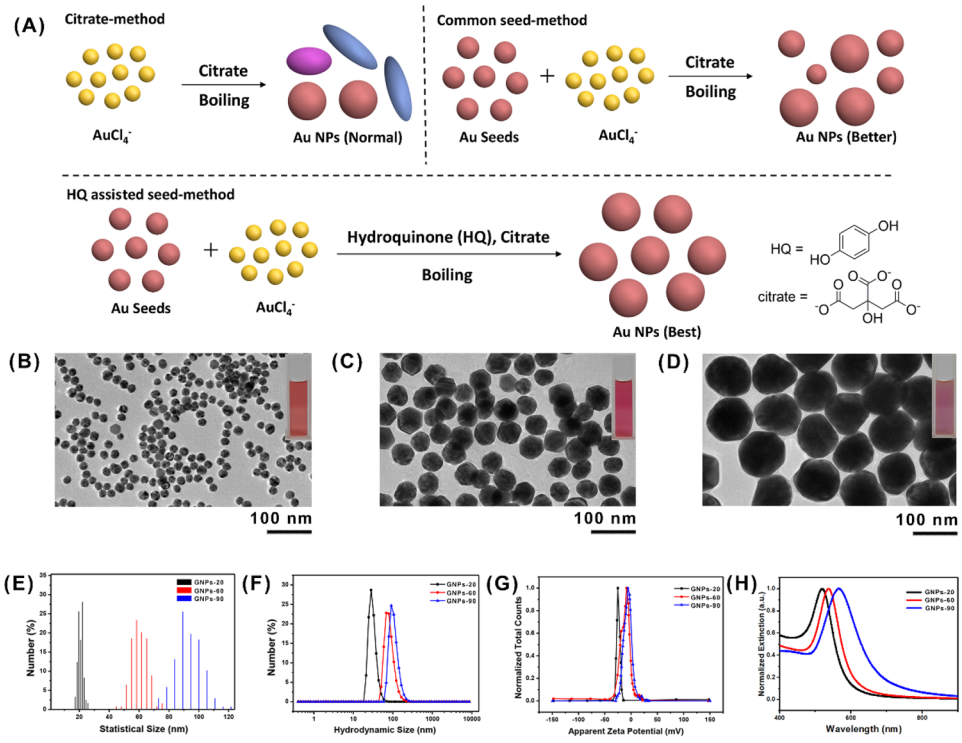

Fig. 1 Characterization of as-prepared GNPs with various sizes. **A** Schematic of hydroquinone-assisted seed-method for preparation of GNPs compared with citrate and common seed-method. **B**–**D** Typical TEM images of GNPs-20, GNPs-60, and GNPs-90 and their corresponding digital photograph (inset) respectively. **E** Statistical size distribution, **F** hydrodynamic size distribution, **G** zeta (ζ) potential, and **H** UV-vis spectra of as-prepared GNPs with three sizes

TEM and SEM observation), PDMS (for AFM observation or biocompatible assessment), and cell culture dish (for osteogenic assessment), which is schematically shown in Fig. 2A. The as-prepared SFGs self-assembled by various sizes of PS-capped GNPs were termed as SFGs-20, SFGs-60, and SFGs-90, respectively. The processes of drying-mediated self-assembly of SFGs are demonstrated in Fig. 2B. In macroscopic view, they took on metallic luster with amaranth, pale-yellow, and bright yellow, respectively (Fig. 2C–E, inset), which could be attributed to the various effective refractive index induced by various size of GNPs. Figure 2C–E demonstrates the TEM images of as-prepared SFGs self-assembled by various sizes of PS-capped GNPs. It could be seen that close-packed one-particle thick arrays were formed with highly ordered structure. Besides, the long-chain PS helps maintain a specific distance between the nanoparticles, preventing the formation of stacked structures. It has been reported that the length of PS chain and the diameter of nanoparticles have remarkable influence on the interparticle spacing of SFGs [39]. After calculation according to the TEM images, a reduced statistical average interparticle spacing could be observed with 17.3 ± 2.7 nm for SFGs-20, 12.7 ± 2.3 nm for SFGs-60, and 11.5 ± 2.3 nm for SFGs-90, respectively.

Similar trends could be found by the observation of SEM (Fig. 2F–H) and AFM images (Fig. 2I–K) with various assembly substrate and synthesis times, indicating that as-prepared SFGs were of great reproducibility and universality for depositing on various substrates (e.g., orthopedic implants). In addition, their reflection spectrum was further detected and the results are demonstrated in Fig. 2L, where it could be seen that a reflection band with the location of 563 nm could be observed for SFGs-20, while relative broad reflection bands located between 700 and 800 nm can be

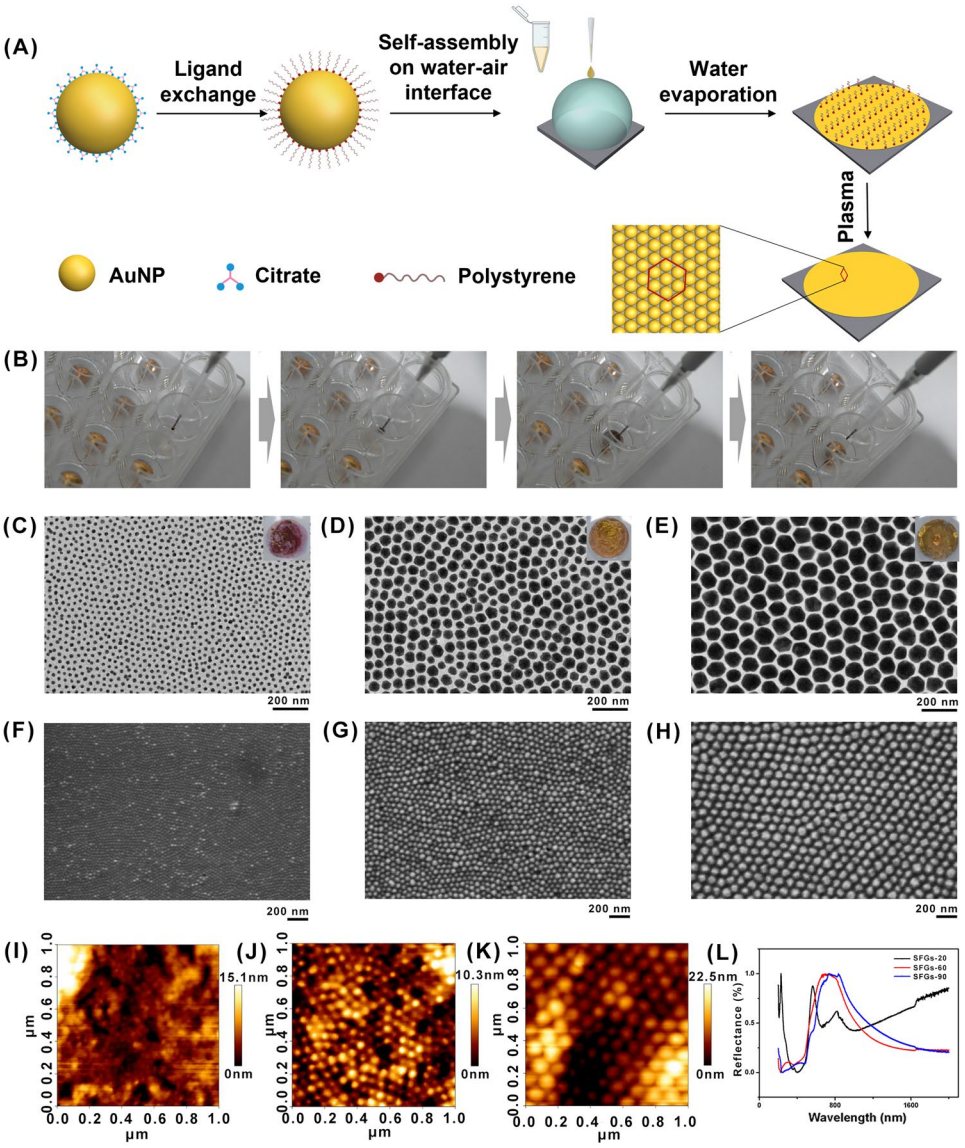

Fig. 2 Characterization of as-prepared SFGs. **A** Schematic diagram and **B** drying-mediated self-assembly process of SFGs. **C–E** Typical TEM images with digital photographs (inset), **F–H** SEM images, and **I–K** AFM images of SFGs-20, SFGs-60, and SFGs-90, respectively. **L** UV-vis-NIR mirror reflection spectra of as-prepared SFGs. Noting that the step peaks located at 720 nm and 830 nm are due to grating conversion of the spectrometer

assigned to SFGs-60 and SFGs-90, respectively. The red-shift of reflection band from SFGs-20 to SFGs-90 was due to the various effective plasmonic coupling induced by the close-packed GNPs. It could be found that the self-assembly process did not largely affect the optical properties of simple gold nanoparticle, indicating that the GNPs were not in the aggregated state. It is noteworthy that as-prepared SFGs were enveloped by large amounts of PS ligands, which may affect their interactions with biological cells. Hence, oxygen plasma treatment was performed to SFGs for short time intervals to partly strip away the surface PS ligands, which was used as spacer molecule to control the interparticle spacing and the exposed time needed to be properly optimized (5 min in this study) to avoid structural disordering [40]. One advantage of SFGs is its universality for depositing on various substrates such as orthopedic implants, which typically used consist of titanium alloy. To verify this, 2D superlattice films of GNPs were assembled onto titanium plate. As illustrated in Supplementary Material, Fig. S1, they exhibited the same metallic luster compared with that self-assembled onto PDMS (Fig. 2C–E, inset). Taken together, the as-prepared SFGs with various surface structures could be used for further biological investigations.

3.3 Biocompatible assessment of SFGs

This study initially aimed to prepare 2D superlattice films of GNPs-PS composites that could be used as a bioactive platform for the surface modification of orthopedic implants to effectively address the problem of aseptic loosening. These films were expected to exhibit excellent biocompatibilities and enhanced osseo-integration abilities (Fig. 3A). Various sizes of GNPs were drying-mediated self-assembled into SFGs on 24-well plates for biocompatible assessment using MC3T3-E1 and RAW264.7 cells as models (Fig. 3B). Live/dead staining was performed to assess the viability of MC3T3-E1 cells treated with SFGs-20, SFGs-60, and SFGs-90 for 24 h, where fluorescent dyes such as PI and calcein AM were used to differentiate living and dead cells based on their membrane integrity. Results demonstrated that similar to the control group (0.08% dead cells), the percentage of the dead cells was almost 0 for each SFGs after 24 h treatment, indicating that all the SFGs are not cytotoxic towards biological cells (Fig. 3C, D). In addition, phalloidin/DAPI staining was also used to visualize the organization of the cytoskeleton and the nuclei of the MC3T3-E1 cells treated with SFGs-20, SFGs-60, and SFGs-90 for 24 h. Phalloidin can specifically bind to F-actin filaments, which is a major structural component of the cytoskeleton, while DAPI is a fluorescent dye that can bind to DNA, allowing the visualization of nuclei within cells. It could be seen that the shapes of MC3T3-E1 cells appeared well in both control and SFGs-treated groups without abnormalities in the nuclei (Fig. 3C). The similar trends could be observed with RAW264.7 cells (Fig. 3E, F). The percentage of dead RAW264.7 cells was 0.68% for SFGs-20, 0.48% for SFGs-60, and 0.11% for SFGs-90, which was similar to the control (0.27% dead cells). The original fluorescence images were shown in Supplementary Material, Figs. S2–S5. These results undoubtedly confirmed that the as-prepared SFGs possess excellent biocompatibility, thus paving the way for further osteogenic differentiation and osteoclast differentiation assessment.

3.4 SFGs stimulates osteogenesis

After confirming the biocompatibility of the SFGs, the effects of SFGs on osteogenic differentiation of MC3T3-E1 cells were assessed using real-time PCR and Western blotting assay. It has been reported that osteogenic differentiation is a complex process involving numerous osteogenesis-associated genes [41]. Hence, MC3T3-E1 cells were treated with SFGs-20, SFGs-60, and SFGs-90 for 3 and 5 days, respectively. Afterwards, the gene expression of multiple osteogenic-related proteins, including OCN, OPN, Col1, Runx2, and ALP, were evaluated. OCN is a major non-collagenous protein in bone exclusively secreted by mature osteoblasts, representing osteogenic differentiation and maturation [42]. As depicted in Fig. 4A, the mRNA expression level of OCN was significantly upregulated after treated with SFGs-90 for 3 and 5 days and SFGs-60 for 5 days compared to the control groups. The same trend was observed with Western blot analysis in Fig. 4F, G, and Supplementary Material, Fig. S7A, B, where the protein expression levels of OCN were elevated in these groups. OPN, another important non-collagenous bone matrix protein, is responsible for bone formation and metabolism [43]. Real-time PCR results revealed significantly increased mRNA expression levels of OPN in the group of SFGs-60 and SFGs-90 at days 7 (Supplementary Material, Fig. S6B).

Furthermore, OPN protein expression levels were demonstrated to increase in all SFGs groups at days 3 and 7 with respect to the control group (Fig. 4F, H, and Supplementary Material, Fig. S7A, C). Col1, an abundant matrix protein secreted by osteoblasts, is a marker of early osteogenesis during bone formation [44]. The stimulating effect was more significant in the cells treated with SFGs-90 compared with the group of SFGs-20 and SFGs-60 as evidenced by results of both mRNA and protein expression levels (Fig. 4C, F, I and Supplementary Material, Fig. S7A, D). Runx2 is a transcriptional factor highly expressed early in osteoblast maturation and controls the differentiation of mesenchymal stem cells to osteoblasts [45]. Runx2 also regulates the expression of many bone-related genes including OCN, OPN, and COL1 [46]. As shown in Fig. 4D, after treatment with SFGs-90 for 3 days, the mRNA expression level of RUNX2 was higher than the control groups.

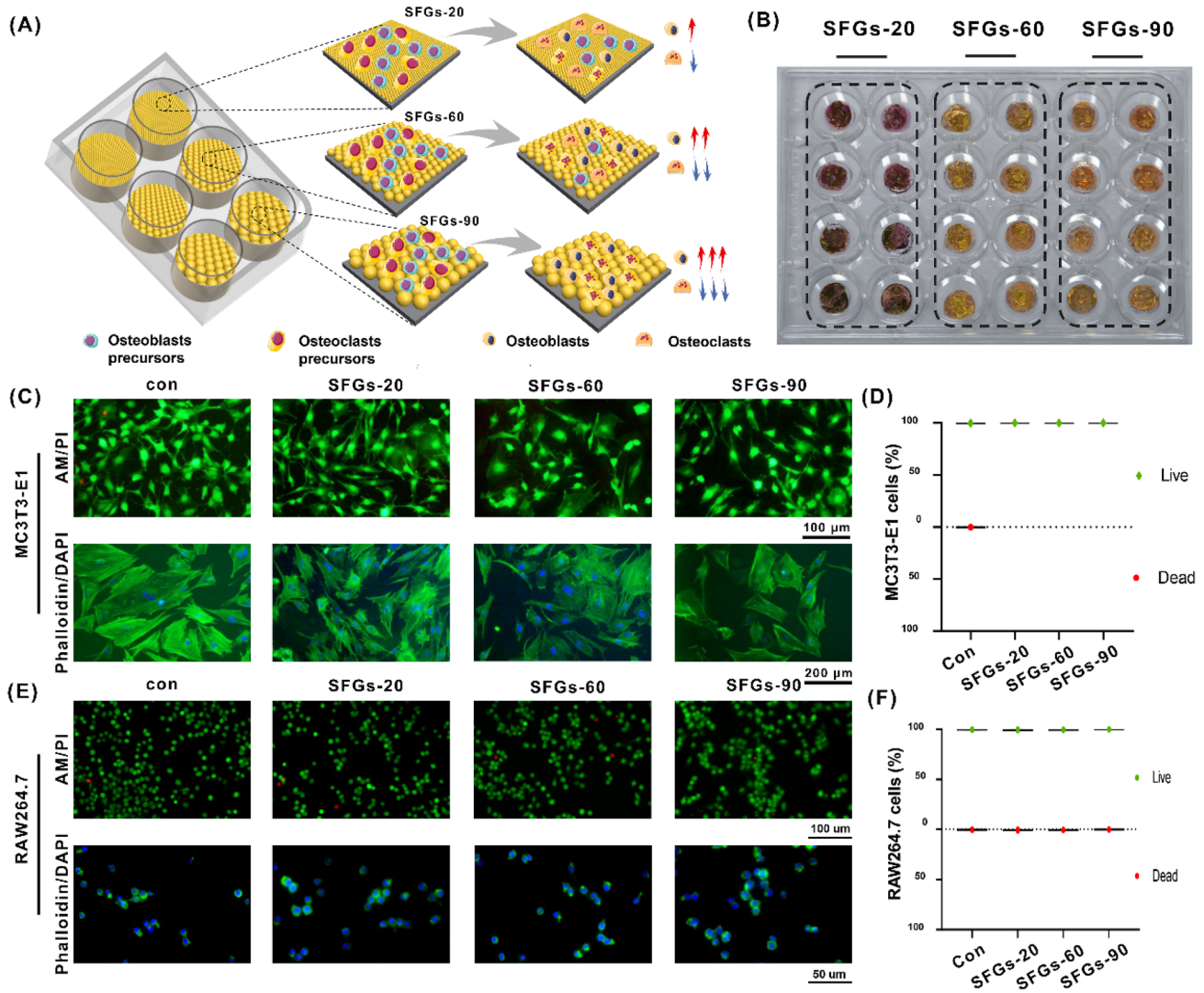

Fig. 3 Biocompatible assessment of as-prepared SFGs. **A** Scheme for in vitro investigations of osteogenic and osteoclast assessment of SFGs. **B** Photograph of various as-prepared SFGs. **C** Representative scan of live/dead staining (green and red labeled cells represent living and dead cells, respectively) and phalloidin/DAPI staining (green and blue labeled cells represent cytoskeleton and nucleus of cells, respectively) of MC3T3-E1 cells after treated with SFGs-20, SFGs-60, and SFGs-90, respectively. **D** Quantification of live/dead staining in Fig. 3C using ImageJ. **E** Representative scan of live/dead staining and phalloidin/DAPI staining of RAW264.7 cells after treated with SFGs-20, SFGs-60, and SFGs-90, respectively. **F** Quantification of live/dead staining in Fig. 3E using ImageJ

Protein expression levels of RUNX2 were significantly upregulated after treated with SFGs-60 and SFGs-90 for 3 and 7 days and SFGs-20 for 3 days (Fig. 4F, K, and Supplementary Material, Fig. S7A, F). In addition, intracellular ALP activity is an early bone marker during osteogenesis [47]. The mRNA expression level of ALP was higher after treated with SFGs-90 for 3 and 7 days, while no statistically significant difference could be observed (Fig. 4E). Protein expression levels of ALP were also significantly upregulated after treated with SFGs-60 and SFGs-90 for 3 and 7 days and SFGs-20 for 3 days (Fig. 4F, J, and Supplementary Material, Fig. S7A, E). The raw WB data are provided as Supplementary Material (Figs. S8 and S9). In order to further verify the early osteogenic differentiation, the effects of SFGs on ALP immunofluorescence staining and ALP activity levels of MC3T3-E1 cells were performed. The ALP quantitative assay could reflect the differentiation level of osteoblasts, higher ALP activity suggests more significant differentiation of pre-osteoblasts into mature osteoblasts [48].

Furthermore, the immunofluorescence detection result of cells showed that ALP expression levels were significantly higher than in controls after treatment of SFGs-20 and SFGs-90 for 7 days (Fig. 5A, B). Moreover, the results of quantification of ALP activity were consistent with those obtained through ALP immunofluorescence

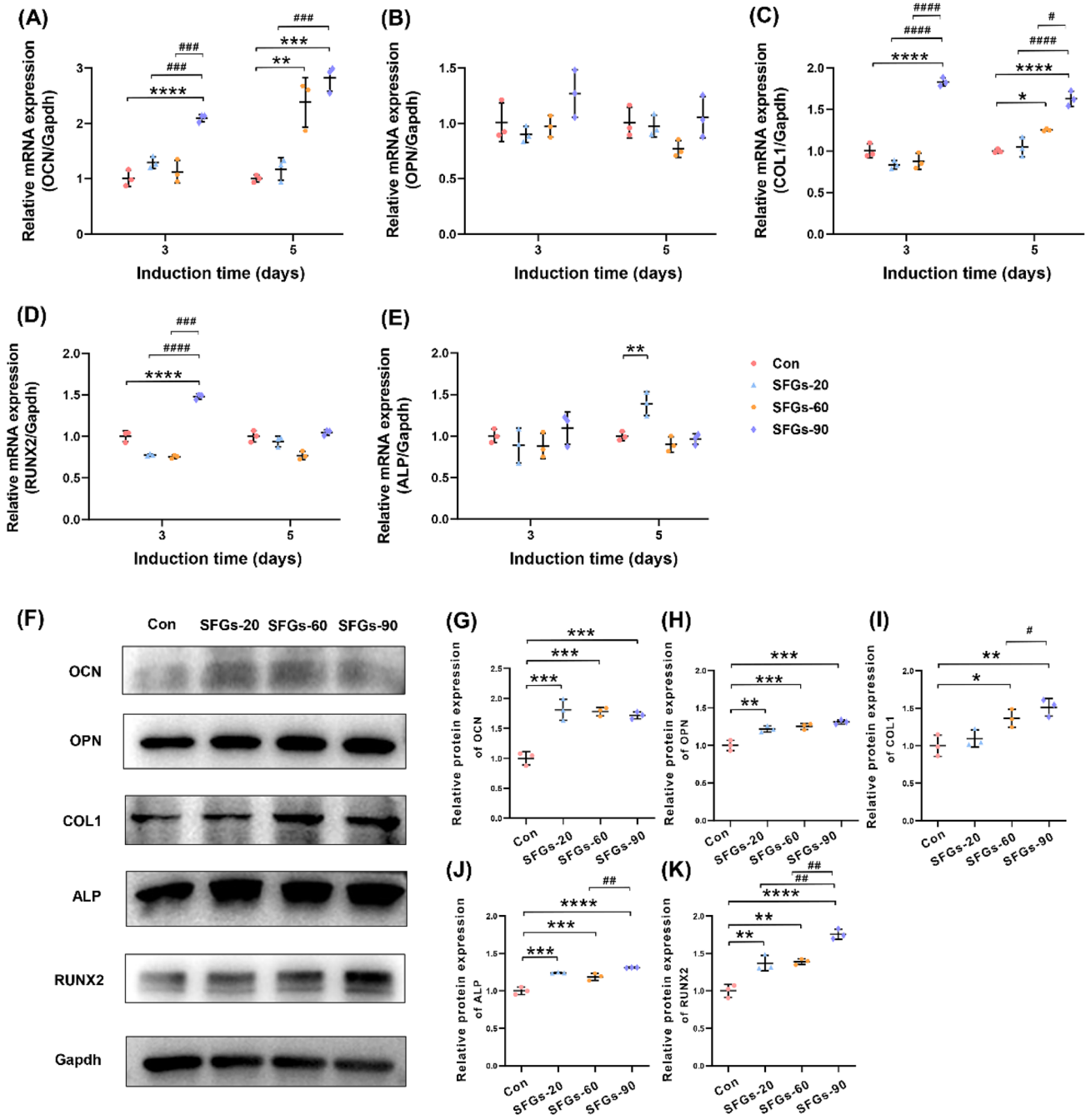

Fig. 4 Effects of SFGs on osteogenic gene expression assayed by real-time PCR and Western blot. **A**–**E** Real-time PCR analysis of OCN, OPN, COL1, ALP, and RUNX2 expressions of MC3T3-E1 cells treated with SFGs-20, SFGs-60, and SFGs-90 for 3 and 5 days, respectively. **F** Western blot analysis and **G**–**K** relative protein level of OCN, OPN, COL1, ALP, and RUNX2 expression of MC3T3-E1 cells after treated with SFGs-20, SFGs-60, and SFGs-90 for 3 days. Asterisk indicates statistically significant differences between the control and experience group (*$p<0.05$; **$p<0.01$; ***$p<0.001$; ****$p<0.0001$), and well numbers (#) indicate statistically significant differences between SFGs-20, SFGs-60, and SFGs-90 (#$p<0.05$; ##$p<0.01$; ###$p<0.001$; ####$p<0.0001$)

staining (Fig. 5C), indicating that SFGs-90 promoted early osteogenesis. These results strongly suggested that SFGs-90 possesses a more robust pro-osteogenic differentiation capacity than SFGs-20 and SFGs-60. The SFGs-90 group consistently exhibited pro-osteogenic effects across multiple experiments, whereas the SFGs-20 and SFGs-60 groups did not demonstrate any significant pro-osteogenic effects in terms of ALP immunofluorescence or ALP activity. All these findings suggested that all the SFGs have certain pro-osteogenic effects, and SFGs-90 has a more pronounced and

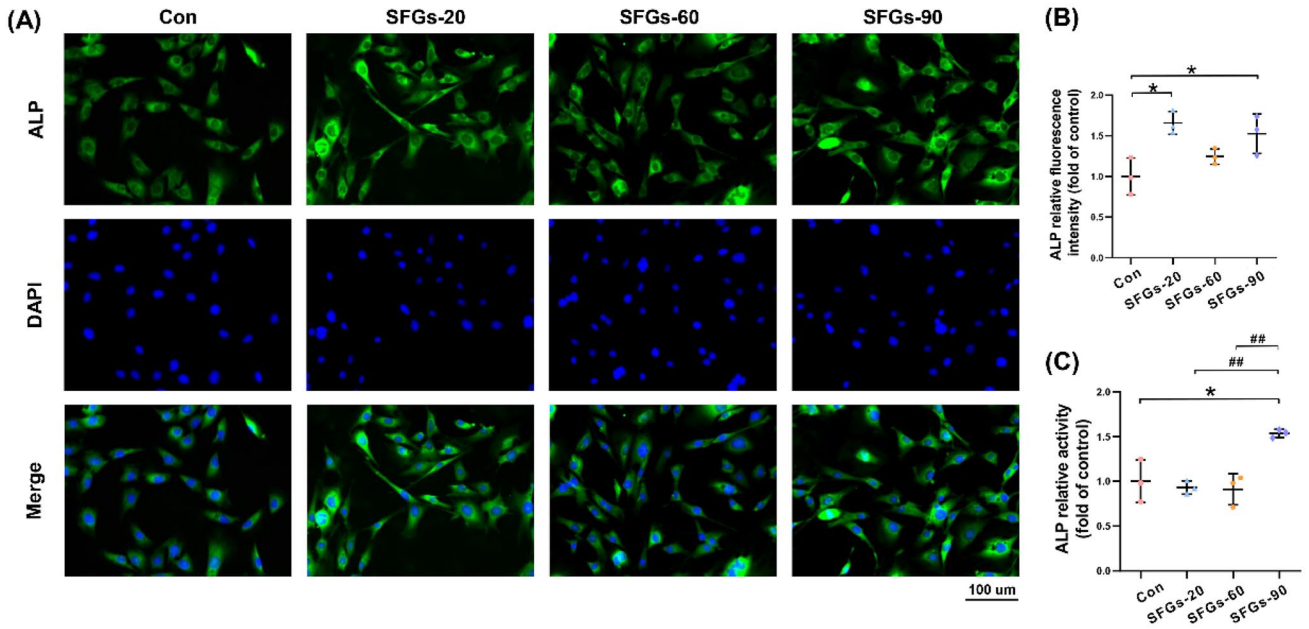

Fig. 5 Osteogenic differentiation assay. **A** MC3T3-E1 cells were cultured on various SFGs in osteogenic medium for 7 days. Cells were stained with DAPI (blue, nuclei staining) and alkaline phosphatase antibodies (green, ALP staining). **B** Quantification of ALP immunofluorescence staining using ImageJ. **C** ALP activity level of MC3T3-E1 cells after treated with SFGs for 7 days. Data expressed as mean ± SD and asterisk indicates statistically significant differences between control and experience group ($*p < 0.05$), and well numbers (#) indicate statistically significant differences between SFGs-20, SFGs-60, and SFGs-90 ($\#\#p < 0.01$)

stable pro-osteogenic differentiation capacity than SFGs-20 and SFGs-60.

3.5 SFGs inhibit osteoclastogenesis

To assess the effects of SFGs on osteoclastic differentiation of biological cells, we employed RAW264.7 cells as model cells, which were cultured under osteoclast differentiation medium. After treatment with various SFGs, the expression of osteoclast-related genes was analyzed. It has been reported that osteoclastic differentiation is a complex process involving numerous osteoclastogenesis-related genes [49]. After 3 and 5 days of treatment with or without SFGs, the expression of osteoclast-related genes, including ATP6vOd2, signaling adaptor protein (TRAF6), osteoclast transcription factors (NFATC1, c-Fos), and bone-resorption enzymes (MMP9, TRAP, and CTSK), were measured in both gene (Fig. 6A–E and Supplementary Material, Fig. S10) and protein levels (Fig. 6F–K). Among these genes, NFATC1 and c-Fos are considered as key transcription factors regarding osteoclastogenesis and bone resorption, where NFATC1 is critical for osteoclast terminal differentiation and c-Fos can activate the expression of NFATC1 [50]. MMP9 as a marker proteinase, released by osteoclasts, reflects the bone resorption status [51]. ATP6vOd2 is highly expressed in osteoclasts and serves a vital role in cell-cell fusion during RANKL-induced osteoclast differentiation [52]. CTSK is a cysteine protease that is predominantly expressed in osteoclasts, which can catabolize collagen, elastin, and gelatin [53]. TRAF6 is a signaling adaptor protein that regulates bone metabolism and inflammatory reaction and the levels of TRAF6 are elevated in diseases such as osteoporosis [54]. TRAP is a specific marker enzyme, which is found mostly in osteoclasts and secreted in large quantities by osteoclasts during bone resorption [55]. The mRNA expression level of NFATC1, c-Fos, TRAP, and MMP9 were significantly decreased compared with the control groups after treated with SFGs-20 for 3 days, while the mRNA expression level of NFATC1, c-Fos, TRAP, MMP9, ATP6vOd2, CTSK, and TRAF6 was significantly decreased compared with the control groups after treated with SFGs-90 for 3 days. Meanwhile, after treated with SFGs-60 for 5 days, the mRNA expression level of NFATC1, c-Fos, TRAP, MMP9, and ATP6vOd2 was significantly decreased compared with the control groups. Besides, the mRNA expression level of NFATC1, c-Fos, MMP9, and ATP6vOd2 was significantly decreased compared with the control groups after treatment of SFGs-20 and SFGs-90 for 5 days. As demonstrated in Fig. 6F–K, the protein expression levels of osteoclast-related genes (NFATC1, c-Fos, TRAF6, and CTSK) were exhibited to decrease in SFGs groups (both SFGs-60 and SFGs-90) for 3 days. The protein expression levels of NFATC1 were also significantly decreased after treated with SFGs-20 for 3 days and the protein expression levels of TRAF6 were

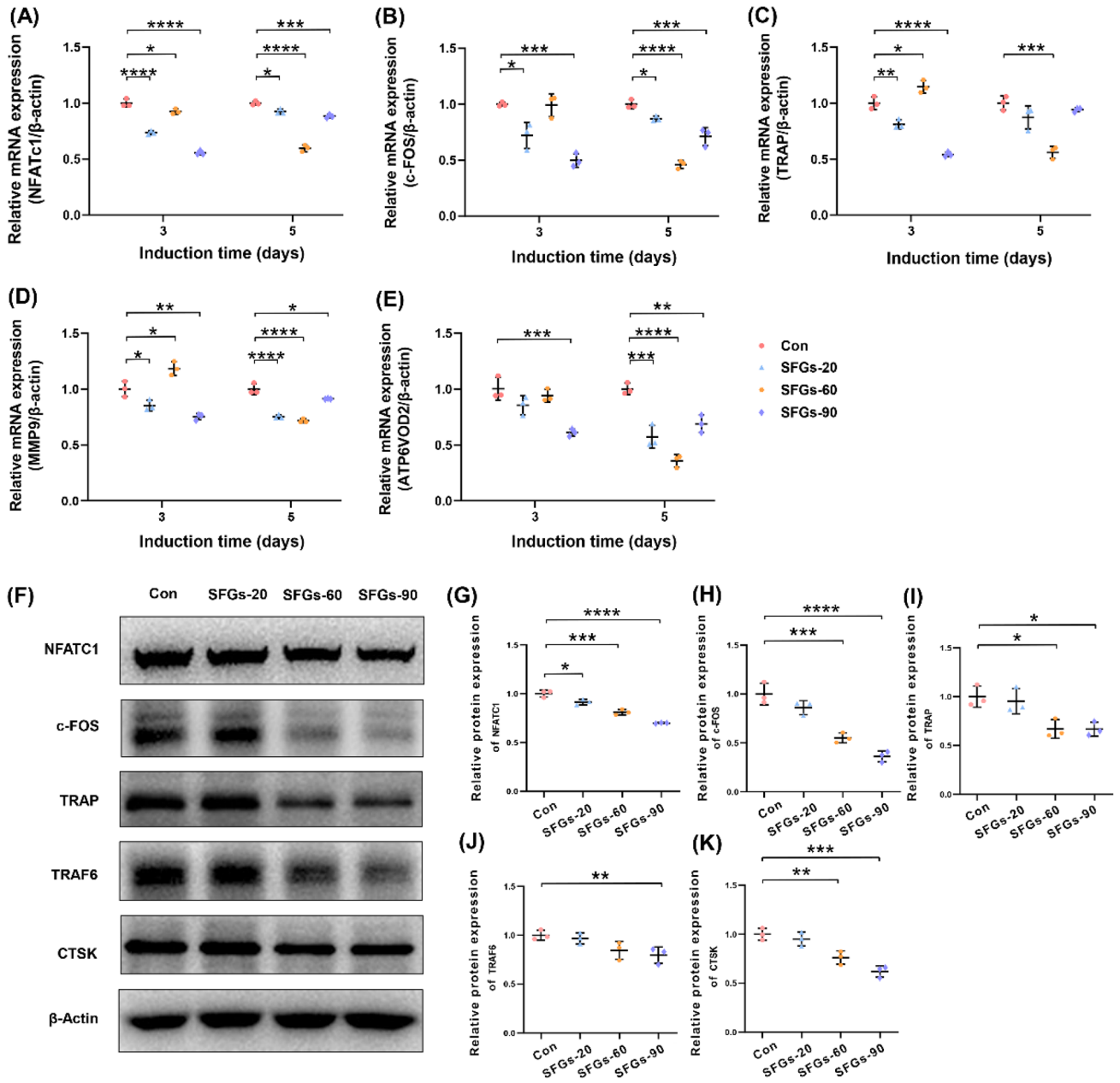

Fig. 6 Effects of SFGs on osteoclastogenesis-related genes expression assayed by real-time PCR and Western blot. **A**–**E** Real-time PCR analysis of NFATC1, c-Fos, TRAP, MMP9, and ATP6VOD2 expressions of RAW264.7 cells treated with SFGs-20, SFGs-60, and SFGs-90 for 3 and 5 days, respectively. **F** Western blot analysis and (G–K) relative protein level of NFATC1, c-Fos, TRAP, TRAF6, and CTSK expression of RAW264.7 cells after treated with SFGs-20, SFGs-60, and SFGs-90 for 3 days, respectively. Asterisk indicates statistically significant differences between control and experience group (*$p < 0.05$; **$p < 0.01$; ***$p < 0.001$; ****$p < 0.0001$)

also significantly decreased after treated with SFGs-90 for 3 days. The raw WB data are provided as Supplementary Material (Fig. S11).

In addition, in order to further verify the osteoclastic-inhibition effects induced by SFGs, BMMs were used as model cells. Adherent BMMs were differentiated into osteoclasts by seeding with MCSF and RANKL either onto SFGs-coated wells or control wells (Fig. 7A). TRAP-positive multinuclear cells (≥ 3 nuclei) were counted as osteoclasts under the fluorescence microscope. Culture of cells treated with SFGs-90 resulted in decreased numbers of multinuclear osteoclasts (Fig. 7B). In addition, the number of nuclei per osteoclast was significantly reduced in SFGs groups (both SFGs-60 and SFGs-90) for 5 days (Fig. 7C). Moreover, as shown in Fig. 7D, after 5 days of culture, the area of the newly formed osteoclasts

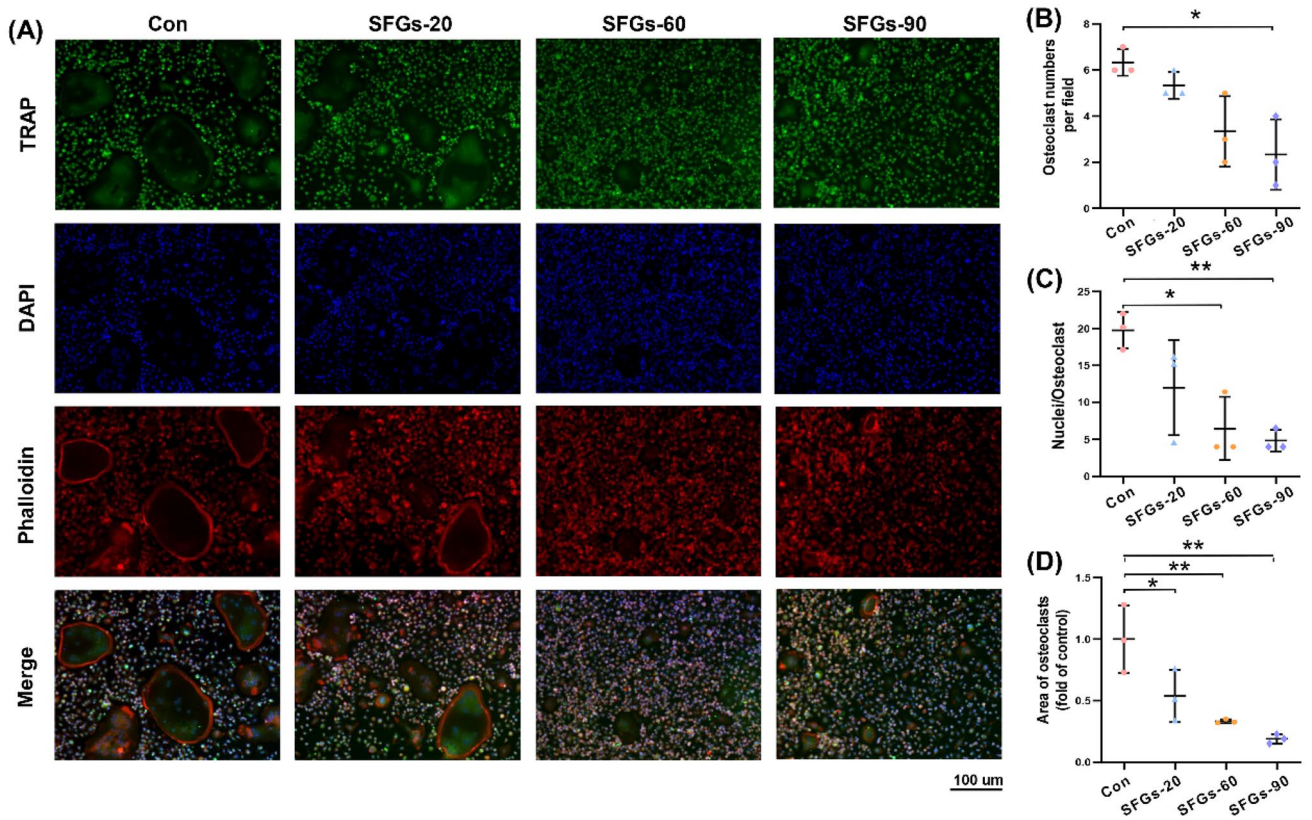

Fig. 7 Osteoclastic differentiation assay. **A** Staining of monocytes from mice after osteoclastic stimulation with various substrates for 5 days. Cells were stained with tartrate-resistant acid phosphatase antibodies (green, TRAP staining), DAPI (blue, nuclei staining), and phalloidin (red, cytoskeleton staining). **B** Mean number of osteoclasts per field. **C** Mean number of nuclei per osteoclast. **D** Quantification of osteoclasts' area using ImageJ. Data expressed as mean ± SD and asterisk indicates statistically significant differences between control and experience group (∗ $p < 0.05$; ∗∗ $p < 0.01$)

was lower in SFGs-treated groups compared with that in the control group, and the osteoclastic-inhibition effect was more significant in the cells treated with SFGs-90, which was consistent with the expression of osteoclastogenesis-related genes results. Taken together, the above findings indicated that all the SFGs have certain anti-osteoclastic effects, where SFGs-90 showed more pronounced and more stable anti-osteoclastic differentiation effects compared with that of SFGs-20 and SFGs-60 in vitro.

4 Conclusion

This study is the first report of macroscopic one-particle thick superlattice films exhibited bone integration-promoting effects. Three sizes of GNPs were prepared and subsequently employed as building blocks for self-assembly of macroscopic one-particle thick superlattice films. Morphological results demonstrated that SFGs possessed highly ordered structures with close-packed one-particle thick arrays. We presented a first attempt to explore the interactions between biological cells and SFGs. Results exhibited that SFGs showed excellent biocompatibility and size-dependent dual effects (osteoclastic-inhibition and osteogenic-stimulation) on maintaining the bone homeostasis. SFGs-90 exhibited the most pronounced facilitation of osteogenic differentiation of osteoblasts as well as deactivation of osteoclasts compared with SFGs-20 and SFGs-60. The universality for depositing on various substrates, excellent biological safety, regulatable morphology and high mechanical strength will benefit the clinical translation of SFGs. These findings shed light on the role of one-particle thick superlattice films in promoting osteogenic differentiation and deactivating osteoclasts. The use of SFGs in orthopedic implants has shown promise in enhancing osseo-integration abilities, which can effectively address the issue of aseptic loosening and offer a new perspective and potential solution for improving the integration of orthopedic implants in bone tissue.

Supplementary Information The online version contains supplementary material available at https://doi.org/10.1007/s42114-023-00738-w.

Author contribution Zaikai Zhuang, Zheng Li, and Guangyu Gong wrote the main manuscript text. Qiangqiang Li and Yibo Zhang performed the biocompatibilities of SFGs. Yusen Huang performed the surface topographical observation of SFGs. Caoxing Huang and Lei Tian revised the manuscript. Peng Wang, Zhirui Guo, and Qing Jiang conceived the idea and designed the research. All authors reviewed the manuscript.

Funding This study was supported by the National Basic Research Program of China (2021YFA1201404), the National Natural Science Foundation of China (32271413, 82202755, and 82172111), Young Scientists Fund of the Natural Science Foundation of Jiangsu Province (BK20220183), and the Top Talents Research Program of the Six-One Project of Jiangsu Province (LGY2019079).

Data availability The data that support the findings of this study are available from the corresponding author, Prof. Qing Jiang, upon reasonable request.

Declarations

Conflict of interest The authors declare no competing interests.

References

1. Ma J, Li ZJ, Xue YZB, Liang XY, Tan ZJ, Tang B (2020) Novel PEEK/nHA composites fabricated by hot-pressing of 3D braided PEEK matrix. Adv Compos Hybrid Mater 3:156–166. https://doi.org/10.1007/s42114-020-00147-3
2. Hodges NA, Sussman EM, Stegemann JP (2021) Aseptic and septic prosthetic joint loosening: Impact of biomaterial wear on immune cell function, inflammation, and infection. Biomaterials 278:121127. https://doi.org/10.1016/j.biomaterials.2021.121127
3. Yao JJ, Lewallen EA, Trousdale WH, Xu W, Thaler R, Salib CG, Reina N, Abdel MP, Lewallen DG, van Wijnen AJ (2017) Local Cellular Responses to Titanium Dioxide from Orthopedic Implants. Biores Open Access 6:94–103. https://doi.org/10.1089/biores.2017.0017
4. Kuang T, Chen S, Gu Z, Shen Z, Hejna A, Saeb MR, Chen F, Zhong M, Liu T (2022) A facile approach to fabricate load-bearing porous polymer scaffolds for bone tissue engineering. Adv Compos Hybrid Mater 5:1376–1384. https://doi.org/10.1007/s42114-022-00418-1
5. Mokhtari S, Eftekhari YB, Marghussian V, Ahmadi PT (2020) Synthesis and characterization of biodegradable AZ31/calcium phosphate glass composites for orthopedic applications. Adv Compos Hybrid Mater 3:390–401. https://doi.org/10.1007/s42114-020-00177-x
6. Al-Harbi NA, Hussein MA, Al-Hadeethi YA, Umar A (2022) Cellulose Acetate-Hydroxyapatite-Bioglass-Zirconia Nanocomposite Particles as Potential Biomaterial: Synthesis, Characterization, and Biological Properties for Bone Application. Eng Sci 17:70–82. https://doi.org/10.30919/es8d528
7. Karazisis D, Ballo AM, Petronis S, Agheli H, Emanuelsson L, Thomsen P, Omar O (2016) The role of well-defined nanotopography of titanium implants on osseointegration: cellular and molecular events in vivo. Int J Nanomedicine 11:1367–1382. https://doi.org/10.2147/ijn.S101294
8. Yue Y, Wang X, Han J, Yu L, Chen J, Wu Q, Jiang J (2019) Effects of nanocellulose on sodium alginate/polyacrylamide hydrogel: Mechanical properties and adsorption-desorption capacities. Carbohydrate Poly 206:289–301. https://doi.org/10.1016/j.carbpol.2018.10.105
9. Pan P, Geng Y, Hu L, Liu Q, Liu M, Cheng M, Chen L, Chen J (2022) Biologically enhanced 3D printed micro-nano hybrid scaffolds doped with abalone shell for bone regeneration. Adv Compos Hybrid Mater 6:10. https://doi.org/10.1007/s42114-022-00593-1
10. Zhang W, Yang P (2019) 2D bio-nanostructures fabricated by supramolecular self-assembly of protein, peptide, or peptoid. Adv Compos Hybrid Mater 2:201–213. https://doi.org/10.1007/s42114-018-0066-x
11. Yeo M, Kim G (2019) Nano/microscale topographically designed alginate/PCL scaffolds for inducing myoblast alignment and myogenic differentiation. Carbohydrate Poly 223:115041. https://doi.org/10.1016/j.carbpol.2019.115041
12. Yuan M, Feng X, Yan T-H, Chen J, Ma X, Cunha P, Lan S, Li Y, Zhou H-C, Wang Y (2022) Superparamagnetic iron oxide-enclosed hollow gold nanostructure with tunable surface plasmon resonances to promote near-infrared photothermal conversion. Adv Compos Hybrid Mater 5:2387–2398. https://doi.org/10.1007/s42114-022-00444-z
13. Wu B, Wang M, Sun Y, Wu F, Shi Z, Wu X (2022) Near-infrared chirality of plasmonic metasurfaces with gold rectangular holes. Adv Compos Hybrid Mater 5:2527–2535. https://doi.org/10.1007/s42114-022-00513-3
14. Chen R, Shi J, Liu C, Li J, Cao S (2022) In situ self-assembly of gold nanorods with thermal-responsive microgel for multi-synergistic remote drug delivery. Adv Compos Hybrid Mater 5:2223–2234. https://doi.org/10.1007/s42114-021-00306-0
15. Shi C, Yuan W, Qu K, Shi J, Eqi M, Tan X, Huang Z, Gándara F, Pan D, Naik N, Zhang Y (2021) Gold/titania Nanorod Assembled Urchin-like Photocatalysts with an Enhanced Hydrogen Generation by Photocatalytic Biomass Reforming. Eng Sci 16:374–386. https://doi.org/10.30919/es8d478
16. Kaur A, Kumar R (2022) Untangling the Effect of Surfactants as An Intermediate at Gold Nanoparticle-Antibiotic Interface for Enhanced Bactericidal Effect. ES Food & Agroforestry 7:30–40. https://doi.org/10.30919/esfaf563
17. Kaur A, Kumar R (2022) Formulation of Biocompatible Vancomycin Conjugated Gold Nanoparticles for Enhanced Antibacterial Efficacy. ES Energy & Environment 15:34–44. https://doi.org/10.30919/esee8c547
18. Zhang Y, Wang P, Mao H, Zhang Y, Zheng L, Yu P, Guo Z, Li L, Jiang Q (2021) PEGylated gold nanoparticles promote osteogenic differentiation in in vitro and in vivo systems. Mater Des 197:109231. https://doi.org/10.1016/j.matdes.2020.109231
19. Huang C, Ye Q, Dong J, Li L, Wang M, Zhang Y, Zhang Y, Wang X, Wang P, Jiang Q (2023) Biofabrication of natural Au/bacterial cellulose hydrogel for bone tissue regeneration via in-situ fermentation. Smart Mater Med 4:1–14. https://doi.org/10.1016/j.smaim.2022.06.001
20. Wang P, Zhang J, Lu Y, Guo Z, Jiang Q, Sun J (2022) DNA-mediated assembly of a gold-nanoparticle film with controllable sonic behavior detected by novel electric-induced ultrasound. Biomater Sci 10:6190–6200. https://doi.org/10.1039/d2bm00778a
21. Xu T, Wang Y, Liu K, Zhao Q, Liang Q, Zhang M, Si C (2023) Ultralight MXene/carbon nanotube composite aerogel for high-performance flexible supercapacitor. Adv Compos Hybrid Mater 6:108. https://doi.org/10.1007/s42114-023-00675-8

22. Liu H, Xu T, Cai C, Liu K, Liu W, Zhang M, Du H, Si C, Zhang K (2022) Multifunctional Superelastic, Superhydrophilic, and Ultralight Nanocellulose-Based Composite Carbon Aerogels for Compressive Supercapacitor and Strain Sensor. Adv Function Mater 32:2113082. https://doi.org/10.1002/adfm.202113082
23. Wang P, Sun J, Lou Z, Fan F, Hu K, Sun Y, Gu N (2016) Assembly-Induced Thermogenesis of Gold Nanoparticles in the Presence of Alternating Magnetic Field for Controllable Drug Release of Hydrogel. Adv Mater 28:10801–10808. https://doi.org/10.1002/adma.201603632
24. Li X, Zhang Y, Liu G, Zhou L, Xue Y, Liu M (2022) Recent progress in the applications of gold-based nanoparticles towards tumor-targeted imaging and therapy. RSC Adv 12:7635–7651. https://doi.org/10.1039/D2RA00566B
25. Fu R, Warnakula T, Shi Q, Yap LW, Dong D, Liu Y, Premaratne M, Cheng W (2020) Plasmene nanosheets as optical skin strain sensors. Nanoscale Horiz 5:1515–1523. https://doi.org/10.1039/D0NH00393J
26. Shi Q, Connell TU, Xiao Q, Chesman ASR, Cheng W, Roberts A, Davis TJ, Gómez DE (2019) Plasmene Metasurface Absorbers: Electromagnetic Hot Spots and Hot Carriers. ACS Photonics 6:314–321. https://doi.org/10.1021/acsphotonics.8b01539
27. Zhang Z, Liu M, Ibrahim MM, Wu H, Wu Y, Li Y, Mersal GAM, El Azab IH, El-Bahy SM, Huang M, Jiang Y, Liang G, Xie P, Liu C (2022) Flexible polystyrene/graphene composites with epsilon-near-zero properties. Adv Compos Hybrid Mater 5:1054–1066. https://doi.org/10.1007/s42114-022-00486-3
28. Xie P, Shi Z, Feng M, Sun K, Liu Y, Yan K, Liu C, Moussa TAA, Huang M, Meng S, Liang G, Hou H, Fan R, Guo Z (2022) Recent advances in radio-frequency negative dielectric metamaterials by designing heterogeneous composites. Adv Compos Hybrid Mater 5:679–695. https://doi.org/10.1007/s42114-022-00479-2
29. Liu M, Wu H, Wu Y, Xie P, Pashameah RA, Abo-Dief HM, El-Bahy SM, Wei Y, Li G, Li W, Liang G, Liu C, Sun K, Fan R (2022) The weakly negative permittivity with low-frequency-dispersion behavior in percolative carbon nanotubes/epoxy nanocomposites at radio-frequency range. Adv Compos Hybrid Mater 5:2021–2030. https://doi.org/10.1007/s42114-022-00541-z
30. Dong D, Fu R, Shi Q, Cheng W (2019) Self-assembly and characterization of 2D plasmene nanosheets. Nat Protoc 14:2691–2706. https://doi.org/10.1038/s41596-019-0200-4
31. Perrault SD, Chan WCW (2009) Synthesis and Surface Modification of Highly Monodispersed, Spherical Gold Nanoparticles of 50–200 nm. J Am Chem Soc 131:17042–17043. https://doi.org/10.1021/ja907069u
32. Walkey CD, Olsen JB, Guo H, Emili A, Chan WC (2012) Nanoparticle size and surface chemistry determine serum protein adsorption and macrophage uptake. J Am Chem Soc 134:2139–2147. https://doi.org/10.1021/ja2084338
33. Fan J, Cheng Y, Sun M (2020) Functionalized Gold Nanoparticles: Synthesis, Properties and Biomedical Applications. Chem Rec 20:1474–1504. https://doi.org/10.1002/tcr.202000087
34. Yeh YC, Creran B, Rotello VM (2012) Gold nanoparticles: preparation, properties, and applications in bionanotechnology. Nanoscale 4:1871–1880. https://doi.org/10.1039/c1nr11188d
35. Makino K, Ohshima H (2010) Electrophoretic Mobility of a Colloidal Particle with Constant Surface Charge Density. Langmuir 26:18016–18019. https://doi.org/10.1021/la1035745
36. Njoki PN, Lim IIS, Mott D, Park H-Y, Khan B, Mishra S, Sujakumar R, Luo J, Zhong C-J (2007) Size Correlation of Optical and Spectroscopic Properties for Gold Nanoparticles. J Phys Chem C 111:14664–14669. https://doi.org/10.1021/jp074902z
37. Liu Z, Shen Y, Wu Y, Yang Y, Wu J, Zhou P, Lu X, Guo Z (2013) An intrinsic therapy of gold nanoparticles in focal cerebral ischemia-reperfusion injury in rats. J Biomed Nanotechnol 9:1017–1028. https://doi.org/10.1166/jbn.2013.1597
38. Liu X, Xu H, Xia H, Wang D (2012) Rapid seeded growth of monodisperse, quasi-spherical, citrate-stabilized gold nanoparticles via H2O2 reduction. Langmuir 28:13720–13726. https://doi.org/10.1021/la3027804
39. Si KJ, Chen Y, Shi Q, Cheng W (2018) Nanoparticle Superlattices: The Roles of Soft Ligands. Adv Sci 5:1700179. https://doi.org/10.1002/advs.201700179
40. Gehl B, Frömsdorf A, Aleksandrovic V, Schmidt T, Pretorius A, Flege JI, Bernstorff S, Rosenauer A, Falta J, Weller H, Bäumer M (2008) Structural and Chemical Effects of Plasma Treatment on Close-Packed Colloidal Nanoparticle Layers. Adv Function Mater 18:2398–2410. https://doi.org/10.1002/adfm.200800274
41. Stein GS, Lian JB (1993) Molecular mechanisms mediating proliferation/differentiation interrelationships during progressive development of the osteoblast phenotype. Endocr Rev 14:424–442. https://doi.org/10.1210/edrv-14-4-424
42. Komori T (2020) Functions of Osteocalcin in Bone, Pancreas, Testis, and Muscle. Int J Mol Sci 21. https://doi.org/10.3390/ijms21207513
43. Icer MA, Gezmen-Karadag M (2018) The multiple functions and mechanisms of osteopontin. Clin Biochem 59:17–24. https://doi.org/10.1016/j.clinbiochem.2018.07.003
44. Butler WT, Brunn JC, Qin C (2009) Dentin Extracellular Matrix (ECM) Proteins: Comparison to Bone ECM and Contribution to Dynamics of Dentinogenesis. Connect Tissue Res 44:171–178. https://doi.org/10.1080/03008200390152287
45. Komori T (2020) Molecular Mechanism of Runx2-Dependent Bone Development. Mol Cells 43:168–175. https://doi.org/10.14348/molcells.2019.0244
46. Inman CK, Shore P (2003) The osteoblast transcription factor Runx2 is expressed in mammary epithelial cells and mediates osteopontin expression. J Biol Chem 278:48684–48689. https://doi.org/10.1074/jbc.M308001200
47. Siller AF, Whyte MP (2018) Alkaline Phosphatase: Discovery and Naming of Our Favorite Enzyme. J Bone Miner Res 33:362–364. https://doi.org/10.1002/jbmr.3225
48. Kokkonen H, Cassinelli C, Verhoef R, Morra M, Schols HA, Tuukkanen J (2008) Differentiation of osteoblasts on pectin-coated titanium. Biomacromol 9:2369–2376. https://doi.org/10.1021/bm800356b
49. Park JH, Lee NK, Lee SY (2017) Current Understanding of RANK Signaling in Osteoclast Differentiation and Maturation. Mol Cells 40:706–713. https://doi.org/10.14348/molcells.2017.0225
50. Kang JY, Kang N, Yang YM, Hong JH, Shin DM (2020) The Role of Ca(2+)-NFATc1 Signaling and Its Modulation on Osteoclastogenesis. Int J Mol Sci 21. https://doi.org/10.3390/ijms21103646
51. Pego ER, Fernandez I, Nunez MJ (2018) Molecular basis of the effect of MMP-9 on the prostate bone metastasis: A review. Urol Oncol 36:272–282. https://doi.org/10.1016/j.urolonc.2018.03.009
52. Lee SH, Rho J, Jeong D, Sul JY, Kim T, Kim N, Kang JS, Miyamoto T, Suda T, Lee SK, Pignolo RJ, Koczon-Jaremko B, Lorenzo J, Choi Y (2006) v-ATPase V0 subunit d2-deficient mice exhibit impaired osteoclast fusion and increased bone formation. Nat Med 12:1403–1409. https://doi.org/10.1038/nm1514
53. Dai R, Wu Z, Chu HY, Lu J, Lyu A, Liu J, Zhang G (2020) Cathepsin K: The Action in and Beyond Bone. Front Cell Dev Biol 8:433. https://doi.org/10.3389/fcell.2020.00433
54. Landstrom M (2010) The TAK1-TRAF6 signalling pathway. Int J Biochem Cell Biol 42:585–589. https://doi.org/10.1016/j.biocel.2009.12.023
55. Ren X, Shan WH, Wei LL, Gong CC, Pei DS (2018) ACP5: Its Structure, Distribution, Regulation and Novel Functions. Anticancer Agents Med Chem 18:1082–1090. https://doi.org/10.2174/1871520618666180411123447